



Cite this: *EES Catal.*, 2023,  
1, 290

## Unlocking nanotubular bismuth oxyiodide toward carbon-neutral electrosynthesis†

Peng-Fei Sui, <sup>a</sup> Min-Rui Gao, <sup>a</sup> Meng-Nan Zhu, <sup>a</sup> Chenyu Xu, <sup>a</sup> Yi-Cheng Wang, <sup>a</sup> Subiao Liu <sup>b</sup> and Jing-Li Luo <sup>\*ac</sup>

The electrochemical  $\text{CO}_2$  reduction reaction ( $\text{CO}_2\text{RR}$ ) to formate is one of the attractive strategies for achieving carbon-neutral sustainability, but synthesizing highly active catalytic materials capable of selectively forming formate, especially under industrially relevant conditions, remains challenging. We herein report ultrathin one-dimensional nanotubular  $\text{Bi}_2\text{O}_7\text{I}$  with substantial amounts of nanopores and oxygen vacancies for the  $\text{CO}_2\text{RR}$ . A desirable selectivity of over 93% and high current density for formate are achieved in a potential window of 1000 mV in a flow cell. More importantly, a stable performance of 140 h with faradaic efficiency over 90% in a membrane electrode assembly system demonstrates great potential for industrial  $\text{CO}_2\text{RR}$  application. The abundant defects within the ultrathin nanotubular structure not only improve the  $\text{CO}_2$  adsorption and charge transfer capabilities that facilitate the reaction kinetics, but also modulate the electronic structure and optimize the energy barrier toward formate as revealed by the theoretical calculations. Concurrently, the local high pH caused by the structural defects and hydrophobic surface could remarkably suppress the hydrogen evolution reaction and in turn, accelerate formate formation. These advances demonstrate an effective structure and defect engineering to unlock one-dimensional electrocatalysts to boost the  $\text{CO}_2\text{RR}$  toward target products.

Received 27th October 2022,  
Accepted 16th February 2023

DOI: 10.1039/d3ey00034f

[rsc.li/eescatalysis](http://rsc.li/eescatalysis)

### Broader context

The conversion of greenhouse gas  $\text{CO}_2$  into value-added chemicals and fuels through electrochemical  $\text{CO}_2$  reduction reaction ( $\text{CO}_2\text{RR}$ ) holds promising potential to reduce the  $\text{CO}_2$  emission level and simultaneously store renewable energy to achieve sustainable carbon neutrality. Given the commercial viability of different reduced products, reducing  $\text{CO}_2$  to formate is one of the most economically viable pathways based on the recent technoeconomic analysis. Nevertheless, achieving high selectivity and current density for formation in a wide potential window still remains challenging when implementing practical  $\text{CO}_2\text{RR}$  technology applications. In this study, we present an effective strategy by introducing abundant defects into the one-dimensional ultrathin nanotubular structure of  $\text{Bi}_2\text{O}_7\text{I}$  for efficient  $\text{CO}_2\text{RR}$  to formate at an industrial-level current density in both flow cell and membrane electrode assembly. The experimental and theoretical studies comprehensively unravel the origins of the enhanced catalytic activity and selectivity resulting from the joint effort of structure and defect merits. These findings underscore the effectiveness of the combination of structure and defect engineering as an attractive strategy for designing advanced electrocatalysts for achieving carbon-neutral sustainability.

## 1. Introduction

The ever-increasing accumulation of  $\text{CO}_2$  in the atmosphere has caused severe climate changes that negatively impact the natural environment and sustainable development of human society.<sup>1–3</sup> The electrochemical  $\text{CO}_2$  reduction reaction ( $\text{CO}_2\text{RR}$ ) is regarded as an attractive technology to lower the  $\text{CO}_2$  emission level when powered by the electricity generated from renewable energy sources (*e.g.*, wind, solar or tidal energy), and it can eventually achieve sustainable carbon neutrality by converting  $\text{CO}_2$  to valuable chemicals.<sup>4–6</sup> However, the inertness of  $\text{CO}_2$  molecules and multi-electron transfer process during the

<sup>a</sup> Department of Chemical and Materials Engineering, University of Alberta, Edmonton, Alberta T6G 1H9, Canada. E-mail: [jingli.luo@ualberta.ca](mailto:jingli.luo@ualberta.ca); Tel: +1 780 492 2232

<sup>b</sup> School of Minerals Processing and Bioengineering, Central South University, Changsha, Hunan, 410083, P. R. China

<sup>c</sup> Shenzhen Key Laboratory of Polymer Science and Technology, College of Materials Science and Engineering, Shenzhen University, Shenzhen 518060, Guangdong, China

† Electronic supplementary information (ESI) available. See DOI: <https://doi.org/10.1039/d3ey00034f>



CO<sub>2</sub>RR usually lead to high thermodynamic energy barriers and sluggish reaction kinetics.<sup>7,8</sup> The low solubility of gaseous CO<sub>2</sub> in aqueous media and broad distributions of target products also account for the unsatisfactory CO<sub>2</sub>RR performance.<sup>9</sup> In addition, the hydrogen evolution reaction (HER) always competes with the CO<sub>2</sub>RR in aqueous media and can significantly deteriorate the selectivity for specific products.<sup>10</sup> Thus, it is of great importance to design highly active and selective electrocatalysts for efficient CO<sub>2</sub>RR.

As one of the typical liquid products with two-electron reduction of CO<sub>2</sub>, formate can be utilized in fuel cells as hydrogen carriers, and in the textile and pharmaceutical industries.<sup>11,12</sup> So far, various metal-based electrocatalysts (e.g., Pd,<sup>13,14</sup> Sn,<sup>15,16</sup> In,<sup>17,18</sup> Pb<sup>19,20</sup> and Bi<sup>21–24</sup>) have been demonstrated to form formate, among which Bi-based materials show great potential due to their low toxicity and earth abundance. Various studies on Bi-based electrocatalysts, including Bi nanoparticles,<sup>25</sup> Bi dendrites<sup>26</sup> and two-dimensional Bi nanosheets,<sup>27–30</sup> have demonstrated the effectiveness of structure engineering in improving CO<sub>2</sub>RR performance toward formate formation, but still fail to meet the requirements of industrial applications, e.g., high current densities ( $j$ ) and wide potential window with high faradaic efficiencies (FEs) to lower the capital investment for the desired production rate.<sup>31,32</sup> However, most of the reported formate faradaic efficiencies (FE<sub>formate</sub>) on Bi-based materials show an increased peak of over 90% at moderate potential, while such high selectivity could only be maintained in a narrow potential window.<sup>33</sup> Although some reported electrocatalysts demonstrated wider potential windows with higher FE<sub>formate</sub>, the achieved  $j$  is still far from the one for practical implementations. Therefore, it is imperative to develop efficient electrocatalysts for CO<sub>2</sub>RR-to-formate conversion with high  $j$  and FE over a wide potential window to realize practical applications at an industrial scale.

It has been well recognized that the structure modulation of electrocatalysts is an effective approach to improving CO<sub>2</sub>RR performance. Among numerous nanomaterials with various morphologies and structures, one-dimensional nanomaterials are regarded as promising candidates for the CO<sub>2</sub>RR.<sup>34,35</sup> The large surface area guarantees a substantial amount of active sites for the CO<sub>2</sub>RR, while the unique channel structure of the nanotubes could significantly improve the charge transfer ability and the mass transport in aqueous media. Nonetheless, electrocatalysts with nanotubular structures are challenging the position to address the issues of low CO<sub>2</sub> solubility and sluggish multi-electron transfer kinetics. As another critical factor, defects on as-prepared electrocatalysts can introduce massive uncoordinated sites, thereby ensuring desirable CO<sub>2</sub>RR performance. Zhang *et al.*<sup>36</sup> demonstrated that defects could enrich the reaction intermediates and OH<sup>–</sup>, which could consequently prompt the C–C bond formation and improve the selectivity of the target product. This is further confirmed by Yang *et al.*<sup>37</sup> who showed that defective indium/indium oxide heterostructures exhibit a high selectivity for C<sub>1</sub> products with FE approaching 100% in a broad potential range. Presently, among various electrocatalysts, defects are mostly introduced on bulk or two-dimensional materials but there are almost no

studies on one-dimensional materials.<sup>38,39</sup> In light of the advantages of low-dimensional materials and structure defects, introducing defects into the nanotubular Bi-based architecture holds great potential to drive highly active and selective CO<sub>2</sub>RR to formate.

In this work, ultrathin Bi<sub>5</sub>O<sub>7</sub>I nanotubes (NTs) with nanopores and abundant oxygen vacancies are synthesized and demonstrated as a highly active, selective and stable electrocatalyst for the CO<sub>2</sub>RR toward formate formation. The as-obtained Bi<sub>5</sub>O<sub>7</sub>I NTs show a desirable FE<sub>formate</sub> within a wide potential range as well as a high formate formation rate of 1145  $\mu\text{mol h}^{-1} \text{cm}^{-2}$  at a moderate potential. Moreover, the CO<sub>2</sub>RR performance is boosted in a flow cell that delivers a high current density of 225 mA cm<sup>–2</sup> at –1.0 V *versus* reversible hydrogen electrode (vs. RHE) and achieves a good stability of 7 h with negligible degradation. The Bi<sub>5</sub>O<sub>7</sub>I NTs are further evaluated in a membrane electrode assembly system at a current density of 200 mA cm<sup>–2</sup> and show negligible changes of cell voltage and FE over 140 h for CO<sub>2</sub>RR. Benefiting from the nanotubular morphology and defective structure, the massive uncoordinated active sites can not only strengthen the CO<sub>2</sub> adsorption and charge transfer, thereby speeding up the CO<sub>2</sub>RR reaction kinetics, but also provide a hydrophobic surface with a higher local pH to effectively inhibit the competing HER. Density functional theory (DFT) calculations reveal that the defective structure of the electrocatalyst can effectively modulate the electronic structure and optimize the adsorption of the reaction intermediate, thereby promoting CO<sub>2</sub>RR performance. All of the above merits collectively contribute to the enhanced electrocatalytic performance for CO<sub>2</sub>-to-formate conversion.

## 2. Results and discussion

### 2.1 Structural characterizations of Bi<sub>5</sub>O<sub>7</sub>I nanotubes

The Bi<sub>5</sub>O<sub>7</sub>I NTs were synthesized *via* the hydrothermal method. As characterized by the high-angle annular dark-field scanning transmission electron microscopy (HAADF-STEM), the prepared catalyst shows an ultrathin nanotubular structure with a uniform diameter of about 5 nm, where a substantial amount of nanopores can be observed on the side wall (Fig. 1a and b). The magnified HAADF-STEM image further clearly shows the wall thickness of about 1 nm with the distribution of nanopores along the wall (Fig. 1c). It is expected that the abundant defects on ultrathin porous nanotubes are beneficial for gas adsorption and charge transfer during the electrochemical reactions. Energy dispersive X-ray spectroscopy (EDS) elemental mapping (Fig. 1d–g) confirms the uniform distribution of Bi, O and I along the nanotubes, indicating a successful preparation of the Bi<sub>5</sub>O<sub>7</sub>I NTs. Moreover, Bi<sub>5</sub>O<sub>7</sub>I NTs were further characterized by powder X-ray diffraction (XRD), as shown in Fig. 1h. The three peaks of the XRD patterns ranging from 25 to 35° are assigned to the (312), (004) and (600) planes of Bi<sub>5</sub>O<sub>7</sub>I (JCPDS 40-0548), suggesting a high purity of the prepared Bi<sub>5</sub>O<sub>7</sub>I NTs. For comparison, Bi<sub>5</sub>O<sub>7</sub>I nanobelts (NBs) were obtained under the same conditions except that the pH was increased to 12.5.



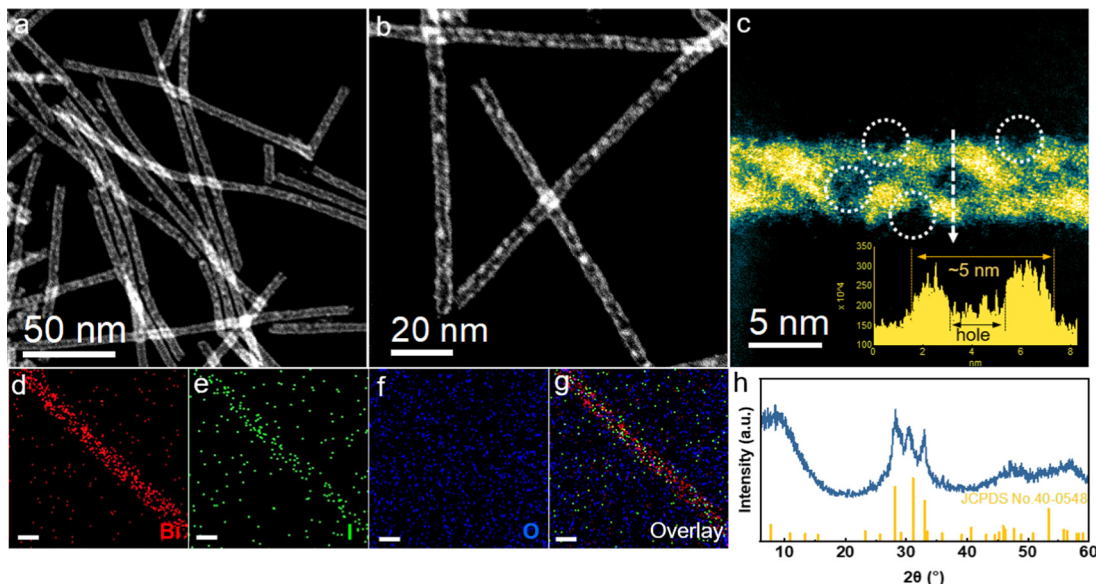


Fig. 1 Catalyst characterizations. (a–c) HADDF-STEM images of  $\text{Bi}_5\text{O}_7\text{I}$  NTs (inset is the line scan of the depth); (d–g) the corresponding EDS elemental mappings and overlay image of  $\text{Bi}_5\text{O}_7\text{I}$  NTs (scale bar: 5 nm); (h) XRD pattern of  $\text{Bi}_5\text{O}_7\text{I}$  NTs.

The scanning electron microscopy (SEM) and TEM images (Fig. S1, ESI<sup>†</sup>) clearly show the structure of belts with the width of around a micrometer, and the lattice fringe of 0.32 nm is assigned to the (312) plane of  $\text{Bi}_5\text{O}_7\text{I}$ , in agreement with the XRD result (Fig. S2, ESI<sup>†</sup>).

## 2.2 Electrocatalytic performance for the $\text{CO}_2\text{RR}$

The  $\text{CO}_2\text{RR}$  electrocatalytic activities of  $\text{Bi}_5\text{O}_7\text{I}$  NTs and NBs were first evaluated in an H-type cell containing 0.5 M  $\text{CO}_2$ -

saturated  $\text{KHCO}_3$  with all the potentials referred to the reversible hydrogen electrode (RHE) unless specified otherwise. Firstly, linear sweep voltammetry (LSV) curves were measured in Ar- and  $\text{CO}_2$ -saturated electrolytes, respectively, to evaluate the electrocatalytic activities toward the  $\text{CO}_2\text{RR}$ . As shown in Fig. 2a, the  $\text{Bi}_5\text{O}_7\text{I}$  NTs deliver a comparably higher total current density ( $j$ ) in  $\text{CO}_2$ -saturated electrolyte than that in Ar, implying the higher preference to the  $\text{CO}_2\text{RR}$ . A similar result is also obtained on  $\text{Bi}_5\text{O}_7\text{I}$  NBs, while the higher  $j$  and more positive

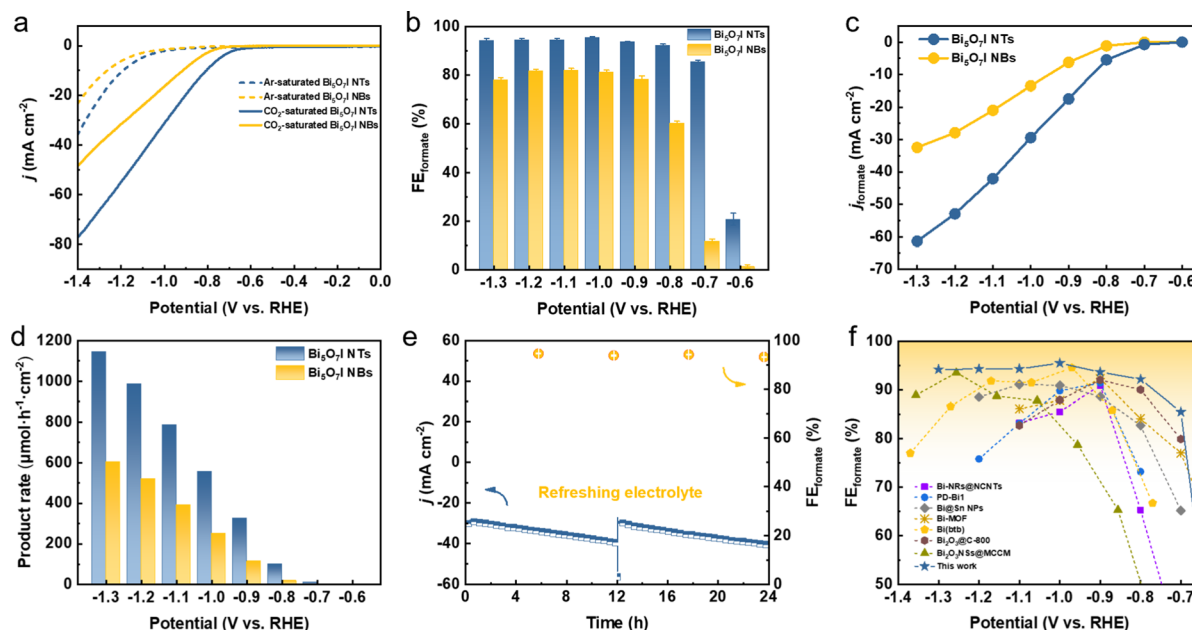


Fig. 2  $\text{CO}_2\text{RR}$  performance in a H-type cell. (a) LSV curves in 0.5 M  $\text{CO}_2$ - or Ar-saturated  $\text{KHCO}_3$  electrolyte, (b) FEs of formate, (c)  $j_{\text{formate}}$  and (d) formate formation rates of  $\text{Bi}_5\text{O}_7\text{I}$  NTs and NBs; (e) stability test of  $\text{Bi}_5\text{O}_7\text{I}$  NTs at  $-1.0$  V in 0.5 M  $\text{CO}_2$ -saturated  $\text{KHCO}_3$  electrolyte; (f) comparison of  $\text{FE}_{\text{formate}}$  of this work with recently reported Bi-based catalysts.

onset potential of the  $\text{Bi}_5\text{O}_7\text{I}$  NTs suggest their better electrocatalytic activity for  $\text{CO}_2$  conversion. To exclude the preferential occurrence of the HER and identify the reduction products of the  $\text{CO}_2\text{RR}$ , controlled electrolysis was carried out (Fig. S3, ESI<sup>†</sup>) at different potentials. The gas-phase products were detected by online gas chromatography (GC), and the liquid products were analyzed by ion chromatography (IC). The results show that formate is the dominating product, together with minor amounts of CO and  $\text{H}_2$ . As displayed in Fig. 2b, the  $\text{Bi}_5\text{O}_7\text{I}$  NTs exhibit higher selectivity for formate formation and the  $\text{FE}_{\text{formate}}$  maintains over 92% in a wide potential range from  $-0.8$  to  $-1.3$  V, whereas  $\text{Bi}_5\text{O}_7\text{I}$  NBs show the inferior selectivity with the maximum  $\text{FE}_{\text{formate}}$  of about 80% under the same applied potentials. Specifically, the maximum  $\text{FE}_{\text{formate}}$  of 95.5% is achieved at  $-1.0$  V where the HER is significantly inhibited with the  $\text{FE}_{\text{H}_2}$  of about 1%. Moreover, the FE<sub>s</sub> for the  $\text{C}_1$  products (*i.e.*, formate and CO) are approaching near-unity within a wide potential gap of 500 mV (Fig. S4, ESI<sup>†</sup>), demonstrating the high preference to the  $\text{CO}_2\text{RR}$  over the competing HER for  $\text{Bi}_5\text{O}_7\text{I}$  NTs.

To reveal the electrocatalytic activity for  $\text{CO}_2\text{RR}$  to formate, the partial current densities of formate ( $j_{\text{formate}}$ ) were derived from the  $j$  and  $\text{FE}_{\text{formate}}$ , as shown in Fig. 2c. Clearly,  $\text{Bi}_5\text{O}_7\text{I}$  NTs possess better electrocatalytic activity for  $\text{CO}_2$ -to-formate conversion, where a  $j_{\text{formate}}$  of about  $61 \text{ mA cm}^{-2}$  was reached at a moderate potential of  $-1.3$  V, about two times higher than that of  $\text{Bi}_5\text{O}_7\text{I}$  NBs ( $32 \text{ mA cm}^{-2}$ ). Fig. 2d shows the formate formation rate, in which  $\text{Bi}_5\text{O}_7\text{I}$  NTs exhibit a rate of  $1145 \mu\text{mol h}^{-1} \text{ cm}^{-2}$  at  $-1.3$  V, comparably higher than  $\text{Bi}_5\text{O}_7\text{I}$  NBs ( $605 \mu\text{mol h}^{-1} \text{ cm}^{-2}$ ). Furthermore, a potentiostatic electrolysis measurement was conducted at  $-1.0$  V on  $\text{Bi}_5\text{O}_7\text{I}$  NTs to evaluate the stability. As shown in Fig. 2e, the  $j$  shows a slight increment after electrolysis for 12 h, which is mainly attributed to the accumulation of products in electrolyte. The  $j$  could go back to the original value after refreshing the electrolyte, indicating the good stability of the electrocatalyst. It is worth noting that the average  $\text{FE}_{\text{formate}}$  was maintained at about 92% over 24 h electrolysis, and this further confirms the remarkable durability of  $\text{Bi}_5\text{O}_7\text{I}$  NTs for formate formation. Further post-catalysis characterizations were performed to identify the structure and composition changes of the catalyst after the  $\text{CO}_2\text{RR}$ . The  $\text{Bi}_5\text{O}_7\text{I}$  NTs are fully reduced to metallic Bi after electrolysis as confirmed by the XRD result (Fig. S5, ESI<sup>†</sup>). It is worth noting that the morphologies of the nanotubular structures with surface defects are well maintained under the reduction conditions, as shown in the TEM images (Fig. S6, ESI<sup>†</sup>). To better demonstrate the reduction of  $\text{Bi}_5\text{O}_7\text{I}$  NTs to defective metallic Bi NTs, an electrochemical activation measurement was conducted using fresh electrode at  $-1.0$  V *vs.* RHE in  $0.5 \text{ M}$   $\text{CO}_2$ -saturated  $\text{KHCO}_3$  for 10 min. The XRD results show that  $\text{Bi}_5\text{O}_7\text{I}$  NTs are already fully reduced to metallic Bi in 10 min (Fig. S7, ESI<sup>†</sup>). From the HRTEM images, some nanopores can be clearly identified on the nanotube walls. The Fourier transform pattern of the selected area belongs to the zone axis [001] where the lattice fringe of  $0.23 \text{ nm}$  is well indexed to the (110) facet of metallic Bi (Fig. S8, ESI<sup>†</sup>). The good structure durability of defective nanotubes

accounts for the negligible degradation of the electrocatalytic performance as well as the good stability. To the best of our knowledge, the electrocatalytic performance of  $\text{Bi}_5\text{O}_7\text{I}$  NTs outperforms the recently reported Bi-based electrocatalysts for the  $\text{CO}_2\text{RR}$  toward formate (Fig. 2f and Table S1, ESI<sup>†</sup>).<sup>23,28,40-44</sup>

Given the reduction of  $\text{Bi}_5\text{O}_7\text{I}$  NTs to defective metallic Bi NTs during the  $\text{CO}_2\text{RR}$ , the similar nanotubular Bi NTs without defects were further prepared to compare the  $\text{CO}_2\text{RR}$  performance. As shown in Fig. S9 (ESI<sup>†</sup>), the high purity of metallic Bi is synthesized using the hydrothermal method. The nested Bi NTs can be clearly observed by SEM and TEM images and the lattice distance of  $0.33 \text{ nm}$  is well indexed to the (012) facet of metallic Bi (Fig. S10, ESI<sup>†</sup>). The EDS result further confirms the successful preparation of Bi NTs. The  $\text{CO}_2\text{RR}$  measurement was conducted under the same conditions as  $\text{Bi}_5\text{O}_7\text{I}$  NTs and NBs. As shown in Fig. S11 (ESI<sup>†</sup>), the selectivity for formate formation is less than 90% in all measured potentials and the maximum  $\text{FE}_{\text{formate}}$  of 86.6% is achieved at  $-1.3$  V *vs.* RHE. In addition, the  $j_{\text{formate}}$  of Bi NTs is much lower compared to that of  $\text{Bi}_5\text{O}_7\text{I}$  NTs, demonstrating the inferior electrocatalytic activity for formate formation.

### 2.3 High-throughput $\text{CO}_2\text{RR}$ performance

It is suggested that the economically compelling application of the  $\text{CO}_2\text{RR}$  toward formate formation requires a minimum  $j$  of  $200 \text{ mA cm}^{-2}$  with the selectivity of 90% to promote the practical  $\text{CO}_2$  electrolysis technology.<sup>32,45</sup> However, the low  $\text{CO}_2$  gas solubility in aqueous media ( $\sim 33 \text{ mM}$ ) strongly restricts the  $\text{CO}_2$  mass transfer, which results in the limited  $j$ . To this end, the  $\text{CO}_2\text{RR}$  performance of  $\text{Bi}_5\text{O}_7\text{I}$  NTs on a gas diffusion electrode (GDE) was evaluated in a flow cell with  $1.0 \text{ M}$  KOH (Fig. S12 and S13, ESI<sup>†</sup>). As shown in Fig. 3a, the onset potential of  $-0.3$  V was reached in the flow cell, much more positive than  $-0.6$  V in the H-type cell. Notably, the  $\text{Bi}_5\text{O}_7\text{I}$  NTs show a high  $j$  of  $390 \text{ mA cm}^{-2}$  at  $-1.4$  V that decreases to about  $225 \text{ mA cm}^{-2}$  at  $-1.0$  V, demonstrating the considerably high electrocatalytic activity for  $\text{CO}_2\text{RR}$ . The shortened gas diffusion pathway on the GDE facilitates the greater access to  $\text{CO}_2$ , resulting in better performance than in the H-type cell. In addition, the reduced ohmic resistance and charge transfer resistance (Fig. S14, ESI<sup>†</sup>) in the flow cell system further promote the enhanced  $\text{CO}_2\text{RR}$  electrocatalytic performance. The potential controlled electrolysis measurements were also conducted, and the results of product analysis suggest that the  $\text{FE}_{\text{formate}}$  exceeds 93% at all the applied potentials from  $-0.3$  to  $-1.3$  V with corresponding  $j_{\text{formate}}$  increasing from  $4.0$  to  $296 \text{ mA cm}^{-2}$  (Fig. 3b). Meanwhile, the  $\text{Bi}_5\text{O}_7\text{I}$  NTs also exhibit a good stability with a high  $j$  of over  $200 \text{ mA cm}^{-2}$  and an average  $\text{FE}_{\text{formate}}$  of about 94% in the flow cell system for 7 h, as shown in Fig. 3c. The high  $\text{FE}_{\text{formate}}$  and  $j$  of  $\text{Bi}_5\text{O}_7\text{I}$  NTs in a wide potential window make it stand out from the recently reported electrocatalysts for formate production in flow cell systems (Table S2, ESI<sup>†</sup>).

To evaluate the feasibility of the actual application of  $\text{Bi}_5\text{O}_7\text{I}$  NTs in the  $\text{CO}_2\text{RR}$  process, a custom-built two-electrode membrane electrode assembly (MEA) system was used to



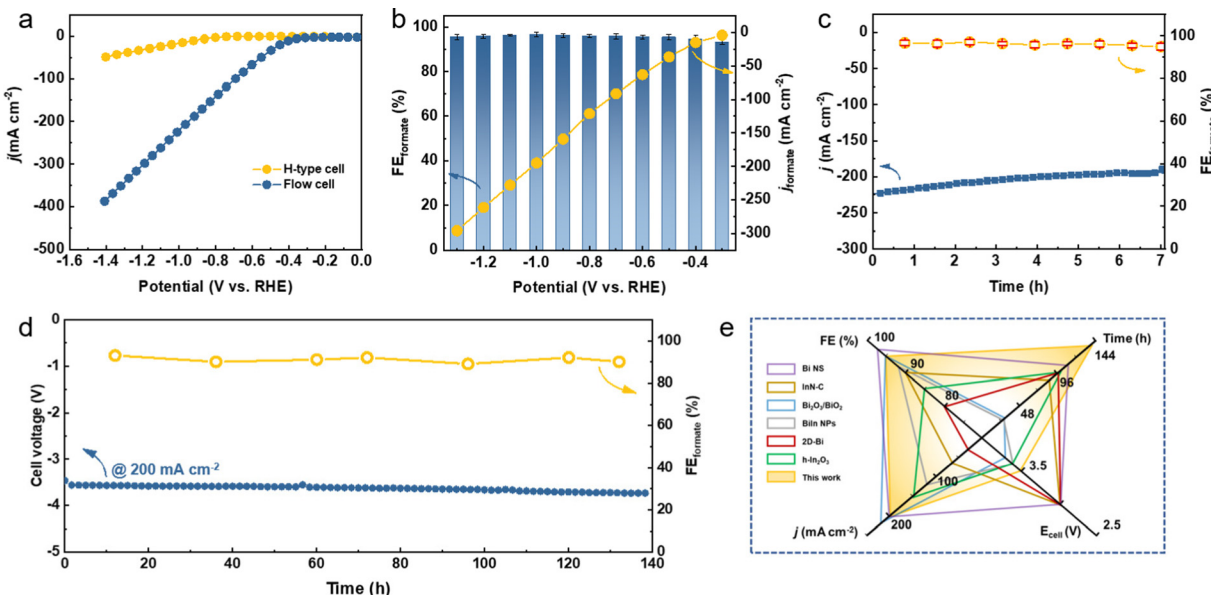


Fig. 3 High-throughput CO<sub>2</sub>RR performance. (a) LSV curves of Bi<sub>5</sub>O<sub>7</sub>I NTs in the H-type cell and flow cell, (b) FE<sub>formate</sub> and  $j_{\text{formate}}$  of Bi<sub>5</sub>O<sub>7</sub>I NTs at all potentials in the flow cell, (c) stability test of Bi<sub>5</sub>O<sub>7</sub>I NTs at -1.0 V vs. RHE in the flow cell, (d) the CO<sub>2</sub>RR performance of Bi<sub>5</sub>O<sub>7</sub>I NTs at 200 mA cm<sup>-2</sup> in the MEA system, and (e) comparison of the FE<sub>formate</sub>,  $E_{\text{cell}}$  and stability of recently reported electrocatalysts for the CO<sub>2</sub>RR to formate in the MEA system.

perform the stability test (Fig. S15, ESI<sup>†</sup>). As shown in Fig. 3d, the electrolysis can be stably operated at 200 mA cm<sup>-2</sup> for 140 h with negligible fluctuation of cell voltage, suggesting the good

stability of the electrocatalyst under the MEA working conditions. Moreover, the FE<sub>formate</sub> was maintained over 90% in the period of 140 h, demonstrating the superb CO<sub>2</sub>RR performance

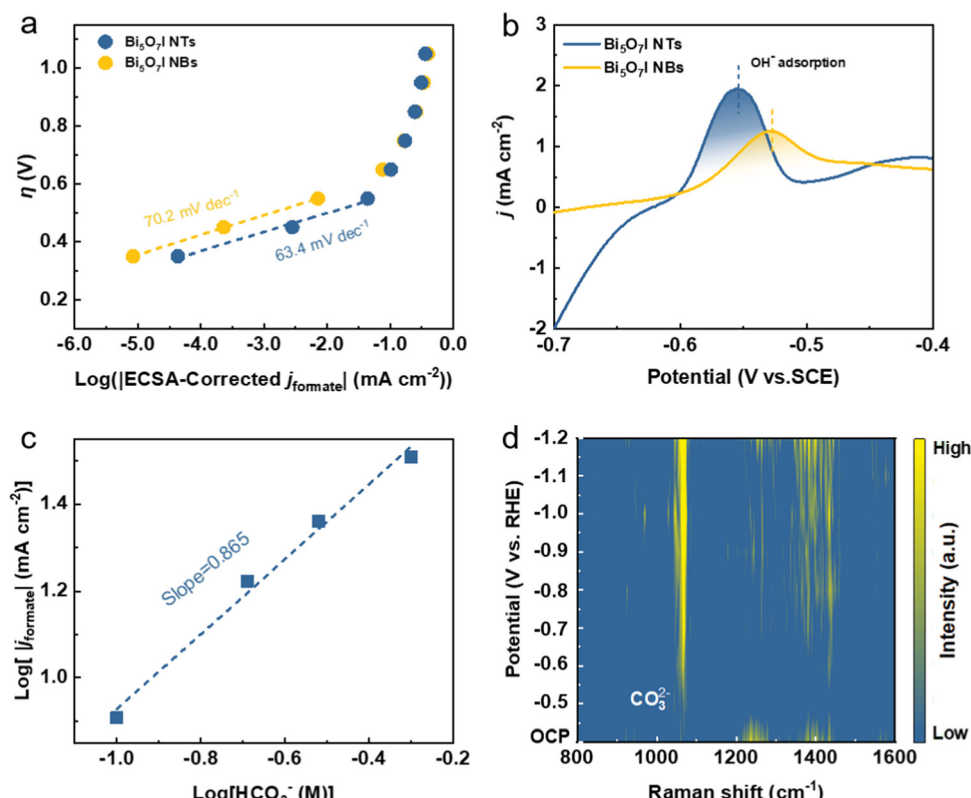


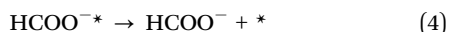
Fig. 4 Kinetic and mechanistic studies. (a) ECSA-corrected Tafel plots for formate production, (b) oxidative LSV curves in N<sub>2</sub>-saturated 0.1 M KOH, (c)  $j_{\text{formate}}$  of Bi<sub>5</sub>O<sub>7</sub>I NTs in different concentrations of HCO<sub>3</sub><sup>-</sup> at -1.0 V vs. RHE, and (d) potential-dependent Raman spectra on Bi<sub>5</sub>O<sub>7</sub>I NTs in 0.5 M CO<sub>2</sub>-saturated KHCO<sub>3</sub>.



of  $\text{Bi}_5\text{O}_7\text{I}$  NTs. Such results make it outperform many recently reported electrocatalysts for  $\text{CO}_2$  to formate conversion in MEA systems (Fig. 3e and Table S3, ESI<sup>†</sup>). Conclusively, the  $\text{Bi}_5\text{O}_7\text{I}$  NTs possess strengthened electrocatalytic activity, selectivity and durability for  $\text{CO}_2$ -to-formate conversion in both the flow cell and MEA systems, thereby demonstrating the promising future for their practical applications in the field of  $\text{CO}_2\text{RR}$  technology.

#### 2.4 Reaction kinetics and mechanistic studies for $\text{CO}_2\text{RR}$ to formate

To investigate the reaction kinetics for  $\text{CO}_2\text{RR}$  to formate formation, Tafel plots were derived based on static state  $j$  and  $\text{FE}_{\text{formate}}$  (Fig. 4a). Compared with  $\text{Bi}_5\text{O}_7\text{I}$  NBs ( $70.2 \text{ mV dec}^{-1}$ ), its smaller Tafel slope of  $63.4 \text{ mV dec}^{-1}$  indicates the faster reaction kinetics process and better stabilization for the  $^*\text{CO}_2^-$  intermediate on  $\text{Bi}_5\text{O}_7\text{I}$  NTs, which ensures the improved  $\text{CO}_2\text{RR}$  performance. It is generally recognized that the rate-determining step (RDS) of formate formation could be identified by matching the theoretical Tafel slopes and experimentally derived values.<sup>46–48</sup> The theoretical Tafel slope of  $118 \text{ mV dec}^{-1}$  suggests the RDS of the initial electron transfer to the adsorbed  $\text{CO}_2$ , *i.e.*,  $^* + \text{CO}_2 + \text{e}^- \rightarrow ^*\text{CO}_2^-$ , where ( $^*$ ) corresponds to the active site for adsorption species, while the value of  $59 \text{ mV dec}^{-1}$  corresponds to the RDS of proton ( $\text{H}^+$ ) transfer served by bicarbonate ( $\text{HCO}_3^-$ ), *i.e.*,  $^*\text{CO}_2^- + \text{HCO}_3^- \rightarrow \text{OCHO}^* + \text{CO}_3^{2-}$ . It is worth noting that the RDS for the  $\text{CO}_2\text{RR}$  toward formate formation is identical for  $\text{Bi}_5\text{O}_7\text{I}$  NTs and NBs, where the Tafel slopes are close to the theoretical value of  $59 \text{ mV dec}^{-1}$ . Therefore, the electroreduction of  $\text{CO}_2$  to formate on  $\text{Bi}_5\text{O}_7\text{I}$  follows the steps below.<sup>11</sup>



It is also noted that the initial electron transfer step to form the intermediate  $^*\text{CO}_2^-$ , *i.e.*, eqn (1), plays a fundamental role for the  $\text{CO}_2\text{RR}$  toward formate. The better stabilization ability of  $^*\text{CO}_2^-$  could facilitate the faster reaction process and improve the selectivity for  $\text{CO}_2$  conversion. To evaluate the binding affinity of  $^*\text{CO}_2^-$  on the catalyst surface, the oxidative LSV measurements were conducted in  $\text{N}_2$ -saturated  $0.1 \text{ M KOH}$  electrolyte where the  $\text{OH}^-$  is considered as the surrogate for  $^*\text{CO}_2^-$ . As shown in Fig. 4b, the  $\text{Bi}_5\text{O}_7\text{I}$  NTs exhibit a higher peak intensity at more negative potential compared to  $\text{Bi}_5\text{O}_7\text{I}$  NBs, an indication of the better adsorption and stabilization capability for the  $^*\text{CO}_2^-$  intermediate and thus, the enhanced  $\text{CO}_2\text{RR}$  performance. The reaction step (2) is further supported by the constant electrolysis performed at  $-1.0 \text{ V vs. RHE}$  with different concentrations of  $\text{KHCO}_3$  electrolyte ranging from  $0.1$  to  $0.5 \text{ M}$  (Fig. S16, ESI<sup>†</sup>). The  $j$  increases with increasing  $[\text{HCO}_3^-]$  so that the  $j$  of  $32.1 \text{ mA cm}^{-2}$  in  $0.5 \text{ M KHCO}_3$  is about four times higher than that of  $8.2 \text{ mA cm}^{-2}$  in  $0.1 \text{ M KHCO}_3$ .

The reaction order with respect to  $\text{HCO}_3^-$  concentration was derived, as displayed in Fig. 4c. It is found that the  $\log j_{\text{formate}}$  shows nearly linear increase with  $\log [\text{HCO}_3^-]$  and the slope of  $0.865$  suggests the first-order relation to  $[\text{HCO}_3^-]$ , in agreement with the result of Tafel slope that  $\text{HCO}_3^-$  serves as the proton donor as the RDS.

The reaction mechanism for the  $\text{CO}_2\text{RR}$  to formate formation was further validated by the *in situ* electrochemical Raman spectroscopy measurement (Fig. S17, ESI<sup>†</sup>). Fig. 4d shows the Raman spectra on  $\text{Bi}_5\text{O}_7\text{I}$  NTs at different applied potentials in  $0.5 \text{ M CO}_2$ -saturated  $\text{KHCO}_3$  electrolyte, in which two obvious peaks are observed at the applied negative potentials. As stated before, the initial electron transfer to form  $^*\text{CO}_2^-$  is the first reaction step during the  $\text{CO}_2\text{RR}$ . The Raman peaks at  $450$  to  $550 \text{ cm}^{-1}$  (Fig. S17c, ESI<sup>†</sup>) start to appear when the applied potential reaches  $-0.6 \text{ V vs. RHE}$ , which are assigned to the peak of carboxylate  $\delta(\text{CO}_2^-)$ .<sup>49</sup> The increased peak intensity suggests the first stage of reaction (1) during the  $\text{CO}_2\text{RR}$ . Moreover, the peak located at about  $1065 \text{ cm}^{-1}$  is ascribed to the symmetric C–O stretching vibration  $\nu_1(\text{CO}_3^{2-})$ ,<sup>50</sup> and the surface weakly adsorbed monodentate carbonate  $\eta^1\text{CO}_3^{2-}$  (Fig. S17d, ESI<sup>†</sup>). It is noted that the peak intensity gradually increases as the applied potential shifts to a more negative range, while no peak is observed when the applied potential is lower than  $-0.6 \text{ V vs. RHE}$ . This demonstrates the occurrence of reaction step (2) during the  $\text{CO}_2\text{RR}$  when the intermediate is formed and accompanied by the production of carbonate ions. Notably, the peaks of  $\delta(\text{CO}_2^-)$  and  $\nu_1(\text{CO}_3^{2-})$  disappear when the applied potential is stopped, further proving that the carbonate intermediate comes from the reaction process (Fig. S18, ESI<sup>†</sup>). All these results provide solid evidence to confirm the reaction mechanism on  $\text{Bi}_5\text{O}_7\text{I}$  NTs for the electroreduction of  $\text{CO}_2$  to formate.

Density functional theory (DFT) calculations were performed to deepen our understanding on the origins of the enhanced catalytic activity and selectivity toward the  $\text{CO}_2\text{RR}$ . Given the full reduction of  $\text{Bi}_5\text{O}_7\text{I}$  NTs to defective metallic Bi NTs during the  $\text{CO}_2\text{RR}$ , the three models of perfect Bi and Bi with different defects were investigated (Bi-V<sub>1</sub> means Bi surface with a mono vacancy and V<sub>2</sub> means di-vacancy). As depicted in Fig. 5a, the charge density difference between Bi and the adsorbate  $^*\text{OCHO}$  on perfect Bi shows relatively low interaction compared to those on Bi-V<sub>1</sub> and Bi-V<sub>2</sub>. The apparent charge transfer between Bi and O atoms on defective Bi demonstrates the stronger interaction of the adsorbate on the Bi surface, which is beneficial for the formation of the  $^*\text{OCHO}$  intermediate. Given the structure difference of Bi, the electronic local functions were further studied (Fig. 5b). The local charge distribution of adjacent Bi atoms can be clearly observed with the existence of defects, which is attributed to the increased orbital overlap caused by the shortened bond length between two adjacent atoms (Fig. S19, ESI<sup>†</sup>), thus resulting in electron delocalization. The p orbital delocalization of the Bi atoms leads to orbital hybridization between the Bi atoms and the adsorbed  $^*\text{OCHO}$ . The more delocalized electrons near the Bi atom with vacancies can effectively promote the formation of the intermediate  $^*\text{OCHO}$ .



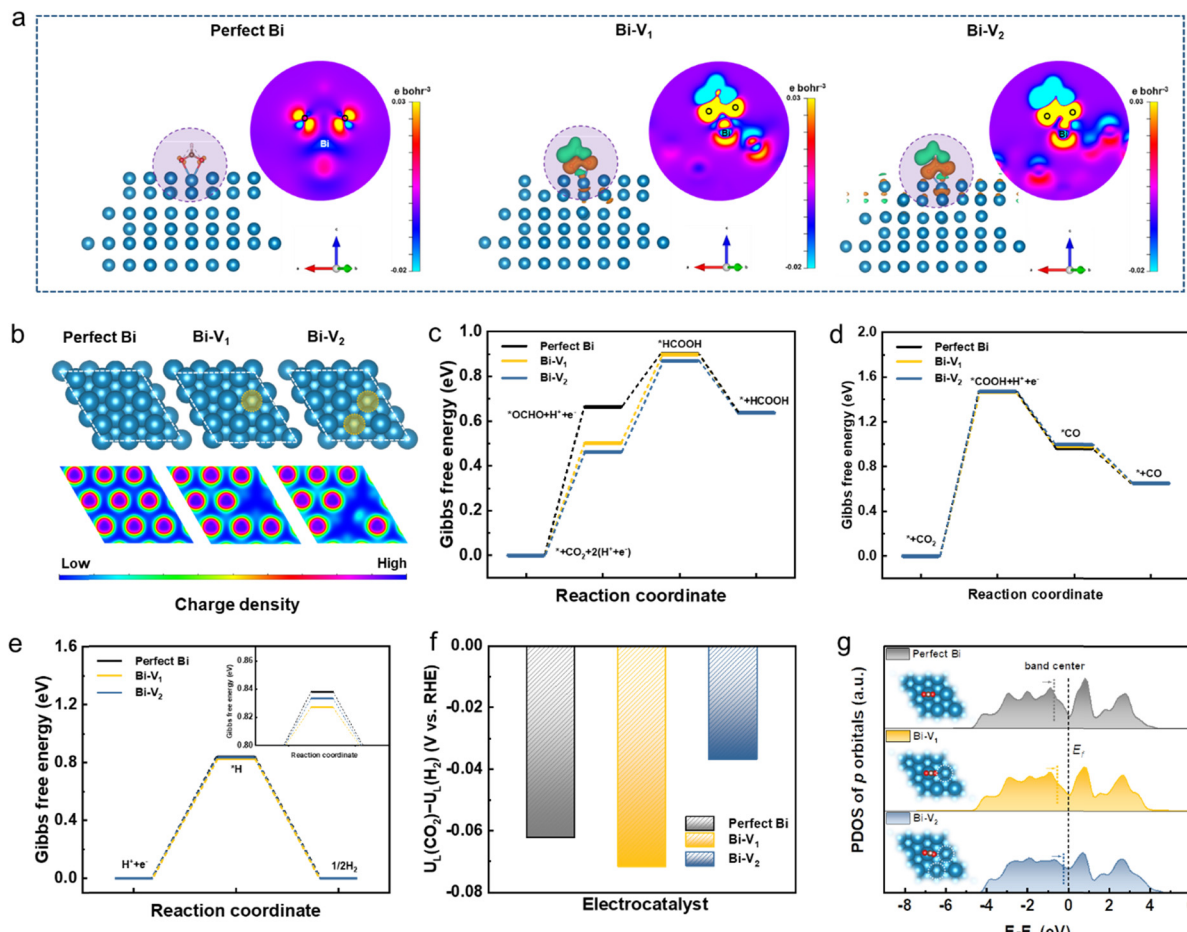


Fig. 5 DFT calculation results. (a) The electron density difference with \*OCHO adsorbates (2D view generated from the plane derived by Bi–O–O atoms), (b) electron local functions, Gibbs free energy of the CO<sub>2</sub>RR to (c) HCOOH pathway and (d) CO pathway, (e) Gibbs free energy of HER, (f) difference in limiting potentials for the CO<sub>2</sub>RR and HER, and (g) the Bi p-PDOS with \*OCHO adsorbates of perfect Bi, Bi-V<sub>1</sub> and Bi-V<sub>2</sub>.

by donating electrons to the reaction, enhancing the interaction between \*OCHO as evidenced by the electron density difference. In addition, the adsorbed intermediate \*OCHO shift to the electron delocalized region on Bi atoms, as shown in Fig. S20 (ESI<sup>†</sup>), further confirming the favorable formation of intermediates over the electron delocalized region.

Furthermore, the Gibbs free energies for CO<sub>2</sub> to HCOOH formation were calculated over the optimized structures shown in Fig. 5c and Fig. S21 (ESI<sup>†</sup>). The formation energy of intermediate \*OCHO decreases from 0.66 to 0.46 eV when introducing a di-vacancy on the Bi, suggesting the lower energy barrier compared to the perfect Bi. The stronger charge interaction between Bi and O atoms and higher local charge distribution near Bi atoms synergistically contribute to better adsorption ability of \*OCHO, leading to the decreased energy barrier in the rate determining step. In addition, the Gibbs free energies for CO<sub>2</sub> to CO formation were also calculated (Fig. 5d and Fig. S22, ESI<sup>†</sup>). It can be found that the rate determining step is the formation of intermediate \*COOH on perfect Bi and defective Bi where no obvious energy difference is observed. The high energy barrier of about 1.47 eV for \*COOH formation is significantly higher than that for \*OCHO formation, leading

to the unfavorable CO formation. Given the competing reaction of the HER during the CO<sub>2</sub>RR, the DFT calculation was further conducted on the HER, as shown in Fig. 5e and Fig. S23 (ESI<sup>†</sup>). When introducing defects on the Bi structure, the Gibbs free energies of the formed \*H display less difference compared to that of perfect Bi. The energy barrier of over 0.8 eV on \*H formation is higher than the rate determining step of \*OCHO formation, indicating the suppression of the HER during the CO<sub>2</sub>RR. Furthermore, the limiting potential difference ( $\Delta U_L$ ) between the CO<sub>2</sub>RR and HER was also determined to reveal the selectivity toward the CO<sub>2</sub>RR. As depicted in Fig. 5f, Bi-V<sub>2</sub> has a more positive potential value (−0.036 V) than perfect Bi (−0.062 V) and Bi-V<sub>1</sub> (−0.072 V), demonstrating the higher selectivity for CO<sub>2</sub> to formate conversion. The projected density of states (PDOS) for Bi p orbitals with adsorbed \*OCHO were plotted where the band center shifts upwards to the Fermi level with increased vacancies, indicating the stronger interaction between \*OCHO and Bi that facilitates the HCOOH formation that also accounts for the high selectivity for CO<sub>2</sub>-to-formate conversion (Fig. 5g). Thus, the vacancies present on Bi can effectively modulate the electronic structure and lower the energy barrier, leading to the superior catalytic performance for the CO<sub>2</sub>RR.



## 2.5 Structural merits of $\text{Bi}_5\text{O}_7\text{I}$ nanotubes towards the enhanced $\text{CO}_2\text{RR}$ performance

To uncover the merits of the defective nanotubular structure, the electrochemical double-layer capacitance ( $C_{\text{dl}}$ ) was measured (Fig. S24, ESI<sup>†</sup>) to determine the electrochemically active surface area (ECSA). As shown in Fig. S25a (ESI<sup>†</sup>), the ultrathin  $\text{Bi}_5\text{O}_7\text{I}$  NTs possess a higher  $C_{\text{dl}}$  ( $6.81 \text{ mF cm}^{-2}$ ) than  $\text{Bi}_5\text{O}_7\text{I}$  NBs ( $3.26 \text{ mF cm}^{-2}$ ), suggesting that the defective nanotubular structure offers a substantial number of active sites and thereby improves the electrocatalytic activity for the  $\text{CO}_2\text{RR}$ . Moreover, the previous study<sup>51–53</sup> also manifests the benefits of the ultrathin nanostructure for  $\text{CO}_2\text{RR}$  performance. The thinner thickness of the electrocatalyst provides higher surface area and more active sites. Compared to the nanobelt structure, the ultrathin nanotube structure of  $\text{Bi}_5\text{O}_7\text{I}$  endows it with larger surface area and more exposed electrocatalytic active sites for the  $\text{CO}_2\text{RR}$  to proceed, which improves both the electrocatalytic activity and selectivity for the conversion of  $\text{CO}_2$  to formate. To exclude the effect of morphology on the  $\text{CO}_2\text{RR}$  performance, the  $j_{\text{formate}}$  was further normalized by the ECSA. As shown in Fig. S25b (ESI<sup>†</sup>), the  $\text{Bi}_5\text{O}_7\text{I}$  NTs still deliver a higher  $j_{\text{formate}}$  compared to  $\text{Bi}_5\text{O}_7\text{I}$  NBs, suggesting the higher intrinsic electrocatalytic activity of the  $\text{Bi}_5\text{O}_7\text{I}$  NTs for the  $\text{CO}_2\text{RR}$  to formate conversion. In addition, the electrochemical impedance spectroscopy (EIS) measurement was conducted to evaluate the charge transfer process between the electrocatalyst and electrolyte. Apparently, the  $\text{Bi}_5\text{O}_7\text{I}$  NTs show comparably smaller interfacial charge transfer resistance compared to NBs (Fig. S26, ESI<sup>†</sup>), indicating a better charge transfer ability to facilitate the occurrence of the  $\text{CO}_2\text{RR}$ . As stated before, the defective nanotubular structure is conducive to gas adsorption, and volumetric  $\text{CO}_2$  adsorption isotherms prove the superb  $\text{CO}_2$  capture ability of  $\text{Bi}_5\text{O}_7\text{I}$  NTs that is three times

higher than that of  $\text{Bi}_5\text{O}_7\text{I}$  NBs (Fig. 6a). The enhanced  $\text{CO}_2$  adsorption capability originates from the abundant nanopores on the ultrathin nanotube wall. This ensures the good mass transfer in aqueous media and benefits the reaction processes on the active sites and consequently, promotes the electrocatalytic performance for formate formation. Aside from the observed nanopores, the result of electron paramagnetic resonance (EPR) measurement displays an obvious signal peak at  $g = 2.001$ , which is ascribed to the oxygen vacancies in  $\text{Bi}_5\text{O}_7\text{I}$  NTs (Fig. 6b). Previous results have demonstrated that the spare electrons at the defect sites of oxygen vacancies could serve as the electron donor to ease the activation of electron-deficient  $\text{CO}_2$  molecules, which is beneficial for the  $\text{CO}_2$  activation to form the  $^*\text{CO}_2^-$ .<sup>38,39,54</sup> This also accounts for the improved electrocatalytic activity over  $\text{Bi}_5\text{O}_7\text{I}$  NTs for  $\text{CO}_2$ -to-formate conversion.

Since the  $\text{CO}_2\text{RR}$  is a proton-coupled electron transfer (PCET) process and the complicated multi-electron transfer steps occur on the catalyst surface, it is important to take the charge transfer ability into consideration to achieve higher activity and selectivity. Work function (WF) is regarded as an effective indicator to describe the electron transfer ability over the catalyst surface. A lower WF corresponds to a higher tunneling probability of electrons, *i.e.*, the electrons are easier to transfer from the catalyst to the reactant and participate in the subsequent reactions of the  $\text{CO}_2\text{RR}$ .<sup>55,56</sup> It can be inferred that the unique channel structure of the nanotubes with abundant nanopores and oxygen vacancies can serve as the charge transport pathway to ensure the faster electron transfer on the catalyst. To this end, the WFs of  $\text{Bi}_5\text{O}_7\text{I}$  NTs and NBs were measured by ultraviolet photoelectron spectroscopy (UPS) as shown in Fig. 6c. Apparently, the defective  $\text{Bi}_5\text{O}_7\text{I}$  NTs possess a lower WF of about 4.75 eV compared to NBs (*i.e.*,

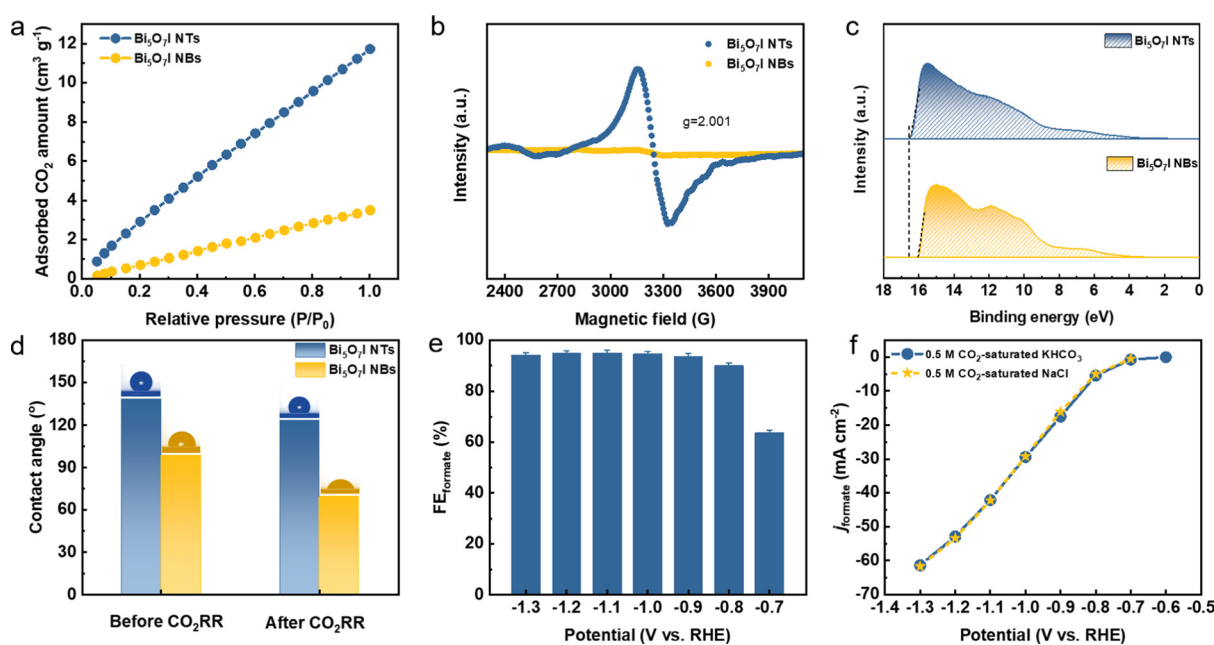


Fig. 6 (a)  $\text{CO}_2$  adsorption isotherms, (b) EPR spectra, (c) UPS spectra and (d) contact angle measurements before and after the  $\text{CO}_2\text{RR}$  on  $\text{Bi}_5\text{O}_7\text{I}$  NTs and NBs, (e)  $\text{FE}_{\text{formate}}$  and (f)  $j_{\text{formate}}$  of  $\text{Bi}_5\text{O}_7\text{I}$  NTs in  $\text{CO}_2$ -saturated 0.5 M  $\text{NaCl}$ .



5.25 eV), demonstrating the enhanced electron transfer ability (Fig. S27, ESI<sup>†</sup>). The fast electron transfer on the catalyst surface facilitates the quick pre-equilibrium of CO<sub>2</sub> to \*CO<sub>2</sub><sup>-</sup>, thereby ensuring the formate formation from the highly selective CO<sub>2</sub>RR.

It is widely accepted that the CO<sub>2</sub>RR is a gas involved reaction and takes place at the triple-phase boundaries. The wettability of the catalyst plays an indispensable role in the reaction process and can consequently tune the product selectivity. Previous studies have suggested that the hydrophobic interface is favorable for formate formation owing to the limited supply of protons to participate in the competitive HER.<sup>57-59</sup> In light of the substantial amount of nanopores on the defective Bi<sub>5</sub>O<sub>7</sub>I NTs, the hydrophobicity is expected across the catalyst surface. Thus, the influence of wettability on CO<sub>2</sub>RR performance was further studied (Fig. S28, ESI<sup>†</sup>). As shown in Fig. 6d, the defective Bi<sub>5</sub>O<sub>7</sub>I NTs present a hydrophobic surface with the contact angle of 138.4°, while a lower hydrophobicity is observed on NBs. After CO<sub>2</sub>RR measurement, the defective nanotubular structure still maintains the hydrophobicity with a slight decrement of the contact angle to 123.5°. Nevertheless, the surface of Bi<sub>5</sub>O<sub>7</sub>I NBs turns out to be hydrophilic with an obvious change of contact angle (Fig. S28d, ESI<sup>†</sup>). The hydrophobic Bi<sub>5</sub>O<sub>7</sub>I NTs can effectively limit the proton supply to suppress the HER, which is consistent with the product distribution result. Concurrently, the enhanced CO<sub>2</sub> adsorption capability can promote sufficient proton donors of HCO<sub>3</sub><sup>-</sup> to enhance the proton-depleted formate formation, thus improving the selectivity of the CO<sub>2</sub>RR. Moreover, the parasitic HER during the CO<sub>2</sub>RR process usually deteriorates the reaction selectivity toward the target product. The research results suggest that the higher local pH near the electrode surface can change the concentrations of proton-donating species and effectively suppress the HER during the CO<sub>2</sub>RR.<sup>36,60,61</sup> It is speculated that a higher local pH could be achieved on the catalyst surface considering the superior hydrophobicity of the Bi<sub>5</sub>O<sub>7</sub>I NTs. To better observe the local pH effect, the phenolphthalein color transition experiment was performed on the prepared catalysts (Fig. S29, ESI<sup>†</sup>). It is found that the defective Bi<sub>5</sub>O<sub>7</sub>I NTs show more significant color change to pink in comparison to the NBs, demonstrating the higher local pH around its surface. This higher pH can lead to a local conversion of CO<sub>2</sub> to HCO<sub>3</sub><sup>-</sup>, *i.e.*, CO<sub>2</sub> + OH<sup>-</sup> → HCO<sub>3</sub><sup>-</sup>, which facilitates the reaction process by providing more proton-donating species and simultaneously suppressing the HER. Based on the above-mentioned, the defective nanotubular structure of Bi<sub>5</sub>O<sub>7</sub>I demonstrates the advantages of creating massive uncoordinated active sites, ensuring the CO<sub>2</sub> adsorption capability and improving the charge transfer capability. Concurrently, the hydrophobic surface with a higher local pH effectively inhibits the HER, thus achieving the selective formation of formate.

## 2.6 CO<sub>2</sub>RR performance in a simulated seawater-based system

It has been shown that most CO<sub>2</sub>RR performance is measured in bicarbonate electrolyte, typically potassium or sodium bicarbonate. To some extent, using low-carbon electrolyte is a promising

approach to reducing the carbon source for the CO<sub>2</sub>RR. Natural seawater is considered as an alternative to substitute the bicarbonate-based electrolyte owing to its abundance and negligible cost.<sup>62,63</sup> The chlorine evolution reaction at the anode can simultaneously produce higher-value products rather than oxygen gas when directly using seawater as the electrolyte for the CO<sub>2</sub>RR. The CO<sub>2</sub>RR performance of defective Bi<sub>5</sub>O<sub>7</sub>I NTs was further evaluated in a 0.5 M NaCl solution that mimics seawater (Fig. S30, ESI<sup>†</sup>). Remarkably, the high FE<sub>formate</sub> is achieved over a wide potential range with a maximum value of 95% that is comparable to the result by using KHCO<sub>3</sub> electrolyte (Fig. 6e). Furthermore, the derived *j*<sub>formate</sub> shows a similar value compared to the measurement in bicarbonate solution, implying the good intrinsic electrocatalytic activity of the Bi<sub>5</sub>O<sub>7</sub>I NTs toward formate formation (Fig. 6f) in a 0.5 M NaCl solution. Therefore, the highly active and selective Bi<sub>5</sub>O<sub>7</sub>I NTs also demonstrate promising prospects for CO<sub>2</sub>RR applications in future seawater-based electrolysis systems.

## 3. Conclusions

Ultrathin Bi<sub>5</sub>O<sub>7</sub>I NTs with abundant nanopores and oxygen vacancies are successfully synthesized and exhibit excellent electrocatalytic performance for the CO<sub>2</sub>RR toward formate with good selectivity and stability, which is further improved in the flow cell and MEA systems by overcoming the limitation of CO<sub>2</sub> mass transport in aqueous media. The high selectivity and current density of formate over a wide potential window, as well as the good stability, make this electrocatalyst a possible candidate for CO<sub>2</sub>RR applications at an industrial scale. The experimental results prove that the nanopores and oxygen vacancies can serve as massive uncoordinated active sites and facilitate the adsorption of CO<sub>2</sub>, which promotes the charge transfer and stabilizes the reaction intermediates toward the CO<sub>2</sub>RR. Theoretical calculations unveil that the existence of defects can effectively modulate the electronic structure, thus benefiting the formation of intermediate \*OHCO toward HCOOH. Furthermore, the hydrophobic catalyst surface with higher local pH effectively suppresses the HER and results in the very efficient performance of the CO<sub>2</sub>RR. These findings highlight the importance of structure and defect engineering as an attractive strategy for designing advanced electrocatalysts for achieving carbon-neutral sustainability.

## Conflicts of interest

The authors declare no conflicts of interest.

## Acknowledgements

This work was supported by the Natural Sciences and Engineering Research Council of Canada, Discovery Grant (GRPIN-2016-05494) and China Scholarship Council. As a part of the University of Alberta's Future Energy Systems research initiative, this research was made possible in part thanks to funding from the Canada First Research Excellence Fund (CFREF-2015-00001).



Thanks to Jiannan Lin for the guidance on materials fabrication. The computation sources are provided by the Digital Research Alliance of Canada (the Alliance).

## References

- 1 G. Wang, J. Chen, Y. Ding, P. Cai, L. Yi, Y. Li, C. Tu, Y. Hou, Z. Wen and L. Dai, *Chem. Soc. Rev.*, 2021, **50**, 4993–5061.
- 2 C. Xu, J. Hong, P. Sui, M. Zhu, Y. Zhang and J.-L. Luo, *Cell Rep. Phys. Sci.*, 2020, **1**, 100101.
- 3 P. De Luna, C. Hahn, D. Higgins, S. A. Jaffer, T. F. Jaramillo and E. H. Sargent, *Science*, 2019, **364**, eaav3506.
- 4 R. Francke, B. Schille and M. Roemelt, *Chem. Rev.*, 2018, **118**, 4631–4701.
- 5 C. Costentin, M. Robert and J. M. Saveant, *Chem. Soc. Rev.*, 2013, **42**, 2423–2436.
- 6 J. Qiao, Y. Liu, F. Hong and J. Zhang, *Chem. Soc. Rev.*, 2014, **43**, 631–675.
- 7 S. Liu, H. Tao, L. Zeng, Q. Liu, Z. Xu, Q. Liu and J. L. Luo, *J. Am. Chem. Soc.*, 2017, **139**, 2160–2163.
- 8 P.-F. Sui, S. Liu, C. Xu, J. Xiao, N. Duan, R. Feng and J.-L. Luo, *Chem. Eng. J.*, 2022, **427**, 131654.
- 9 T. Burdyny and W. A. Smith, *Energy Environ. Sci.*, 2019, **12**, 1442–1453.
- 10 Y. Y. Birdja, E. Pérez-Gallent, M. C. Figueiredo, A. J. Göttle, F. Calle-Vallejo and M. T. M. Koper, *Nat. Energy*, 2019, **4**, 732–745.
- 11 N. Han, P. Ding, L. He, Y. Li and Y. Li, *Adv. Energy Mater.*, 2019, 1902338.
- 12 M. F. Philips, G.-J. M. Gruter, M. T. M. Koper and K. J. P. Schouten, *ACS Sustainable Chem. Eng.*, 2020, **8**, 15430–15444.
- 13 T. Gunji, H. Ochiai, T. Ohira, Y. Liu, Y. Nakajima and F. Matsumoto, *Chem. Mater.*, 2020, **32**, 6855–6863.
- 14 N. Han, M. Sun, Y. Zhou, J. Xu, C. Cheng, R. Zhou, L. Zhang, J. Luo, B. Huang and Y. Li, *Adv. Mater.*, 2021, **33**, 2005821.
- 15 Z. Chen, T. Fan, Y.-Q. Zhang, J. Xiao, M. Gao, N. Duan, J. Zhang, J. Li, Q. Liu, X. Yi and J.-L. Luo, *Appl. Catal., B*, 2020, **261**, 118243.
- 16 S. Liu, J. Xiao, X. F. Lu, J. Wang, X. Wang and X. W. D. Lou, *Angew. Chem., Int. Ed.*, 2019, **58**, 8499–8503.
- 17 Y. Huang, X. Mao, G. Yuan, D. Zhang, B. Pan, J. Deng, Y. Shi, N. Han, C. Li, L. Zhang, L. Wang, L. He, Y. Li and Y. Li, *Angew. Chem., Int. Ed.*, 2021, **60**, 15844–15848.
- 18 W. Guo, X. Tan, J. Bi, L. Xu, D. Yang, C. Chen, Q. Zhu, J. Ma, A. Tayal, J. Ma, Y. Huang, X. Sun, S. Liu and B. Han, *J. Am. Chem. Soc.*, 2021, **143**, 6877–6885.
- 19 M. J. W. Blom, V. Smulders, W. P. M. van Swaaij, S. R. A. Kersten and G. Mul, *Appl. Catal., B*, 2020, **268**, 118420.
- 20 C. H. Lee and M. W. Kanan, *ACS Catal.*, 2014, **5**, 465–469.
- 21 P. Deng, H. Wang, R. Qi, J. Zhu, S. Chen, F. Yang, L. Zhou, K. Qi, H. Liu and B. Y. Xia, *ACS Catal.*, 2019, **10**, 743–750.
- 22 C. W. Lee, J. S. Hong, K. D. Yang, K. Jin, J. H. Lee, H.-Y. Ahn, H. Seo, N.-E. Sung and K. T. Nam, *ACS Catal.*, 2018, **8**, 931–937.
- 23 S. Liu, X. F. Lu, J. Xiao, X. Wang and X. W. D. Lou, *Angew. Chem., Int. Ed.*, 2019, **58**, 13828–13833.
- 24 P. F. Sui, C. Xu, M. N. Zhu, S. Liu, Q. Liu and J. L. Luo, *Small*, 2021, e2105682.
- 25 Y. Qiu, J. Du, W. Dong, C. Dai and C. Tao, *J. CO<sub>2</sub> Util.*, 2017, **20**, 328–335.
- 26 J. H. Koh, D. H. Won, T. Eom, N.-K. Kim, K. D. Jung, H. Kim, Y. J. Hwang and B. K. Min, *ACS Catal.*, 2017, **7**, 5071–5077.
- 27 F. P. Garcia de Arquer, O. S. Bushuyev, P. De Luna, C. T. Dinh, A. Seifitokaldani, M. I. Saidaminov, C. S. Tan, L. N. Quan, A. Proppe, M. G. Kibria, S. O. Kelley, D. Sinton and E. H. Sargent, *Adv. Mater.*, 2018, **30**, e1802858.
- 28 Y. Wang, Y. Li, J. Liu, C. Dong, C. Xiao, L. Cheng, H. Jiang, H. Jiang and C. Li, *Angew. Chem., Int. Ed.*, 2021, **60**, 7681–7685.
- 29 J. Yang, X. Wang, Y. Qu, X. Wang, H. Huo, Q. Fan, J. Wang, L. M. Yang and Y. Wu, *Adv. Energy Mater.*, 2020, **10**, 2001709.
- 30 W. Ma, J. Bu, Z. Liu, C. Yan, Y. Yao, N. Chang, H. Zhang, T. Wang and J. Zhang, *Adv. Funct. Mater.*, 2020, 2006704.
- 31 Y. Cheng, P. Hou, X. Wang and P. Kang, *Acc. Chem. Res.*, 2022, **55**, 231–240.
- 32 R. I. Masel, Z. Liu, H. Yang, J. J. Kaczur, D. Carrillo, S. Ren, D. Salvatore and C. P. Berlinguette, *Nat. Nanotechnol.*, 2021, **16**, 118–128.
- 33 Y. Guan, M. Liu, X. Rao, Y. Liu and J. Zhang, *J. Mater. Chem. A*, 2021, **9**, 13770–13803.
- 34 A. Guan, C. Yang, Y. Quan, H. Shen, N. Cao, T. Li, Y. Ji and G. Zheng, *Chem. – Asian J.*, 2019, **14**, 3969–3980.
- 35 S. P. Paula, M. Stefano, E. L. S. Ifan and E. E. María, *ChemCatChem*, 2019, **11**, 1–21.
- 36 B. Zhang, J. Zhang, M. Hua, Q. Wan, Z. Su, X. Tan, L. Liu, F. Zhang, G. Chen, D. Tan, X. Cheng, B. Han, L. Zheng and G. Mo, *J. Am. Chem. Soc.*, 2020, **142**, 13606–13613.
- 37 W. Yang, Y. Zhao, S. Chen, W. Ren, X. Chen, C. Jia, Z. Su, Y. Wang and C. Zhao, *Inorg. Chem.*, 2020, **59**, 12437–12444.
- 38 Q. Wang, Y. Lei, D. Wang and Y. Li, *Energy Environ. Sci.*, 2019, **12**, 1730–1750.
- 39 Y. Wang, P. Han, X. Lv, L. Zhang and G. Zheng, *Joule*, 2018, **2**, 2551–2582.
- 40 W. Zhang, S. Yang, M. Jiang, Y. Hu, C. Hu, X. Zhang and Z. Jin, *Nano Lett.*, 2021, **21**, 2650–2657.
- 41 Y. Xing, X. Kong, X. Guo, Y. Liu, Q. Li, Y. Zhang, Y. Sheng, X. Yang, Z. Geng and J. Zeng, *Adv. Sci.*, 2020, 1902989.
- 42 P. Deng, F. Yang, Z. Wang, S. Chen, Y. Zhou, S. Zaman and B. Y. Xia, *Angew. Chem., Int. Ed.*, 2020, **59**, 10807–10813.
- 43 F. Li, G. H. Gu, C. Choi, P. Kolla, S. Hong, T.-S. Wu, Y.-L. Soo, J. Masa, S. Mukerjee, Y. Jung, J. Qiu and Z. Sun, *Appl. Catal., B*, 2020, **277**, 119241.
- 44 P. Lamagni, M. Miola, J. Catalano, M. S. Hvid, M. A. H. Mamakhel, M. Christensen, M. R. Madsen, H. S. Jeppesen, X. M. Hu, K. Daasbjerg, T. Skrydstrup and N. Lock, *Adv. Funct. Mater.*, 2020, 1910408.
- 45 H. Rabiee, L. Ge, X. Zhang, S. Hu, M. Li and Z. Yuan, *Energy Environ. Sci.*, 2021, **14**, 1959–2008.
- 46 C. W. Lee, N. H. Cho, S. W. Im, M. S. Jee, Y. J. Hwang, B. K. Min and K. T. Nam, *J. Mater. Chem. A*, 2018, **6**, 14043–14057.

- 47 A. Wuttig, Y. Yoon, J. Ryu and Y. Surendranath, *J. Am. Chem. Soc.*, 2017, **139**, 17109–17113.
- 48 S. Zhang, P. Kang and T. J. Meyer, *J. Am. Chem. Soc.*, 2014, **136**, 1734–1737.
- 49 C. He, S. Chen, R. Long, L. Song and Y. Xiong, *Sci. China: Chem.*, 2020, **63**, 1721–1726.
- 50 I. V. Chernyshova, P. Somasundaran and S. Ponnurangam, *Proc. Natl. Acad. Sci. U. S. A.*, 2018, **115**, E9261–E9270.
- 51 N. Han, Y. Wang, H. Yang, J. Deng, J. Wu, Y. Li and Y. Li, *Nat. Commun.*, 2018, **9**, 1320.
- 52 F. Yang, A. O. Elnabawy, R. Schimmenti, P. Song, J. Wang, Z. Peng, S. Yao, R. Deng, S. Song, Y. Lin, M. Mavrikakis and W. Xu, *Nat. Commun.*, 2020, **11**, 1088.
- 53 P. Su, W. Xu, Y. Qiu, T. Zhang, X. Li and H. Zhang, *ChemSusChem*, 2018, **11**, 848–853.
- 54 Z. Wu, Y. Zhao, W. Jin, B. Jia, J. Wang and T. Ma, *Adv. Funct. Mater.*, 2020, 2009070.
- 55 Z.-Z. Wu, F.-Y. Gao and M.-R. Gao, *Energy Environ. Sci.*, 2021, **14**, 1121–1139.
- 56 P. F. Sui, M. R. Gao, S. Liu, C. Xu, M. N. Zhu and J. L. Luo, *Adv. Funct. Mater.*, 2022, 2203794.
- 57 P. Yue, Q. Fu, J. Li, L. Zhang, L. Xing, Z. Kang, Q. Liao and X. Zhu, *Chem. Eng. J.*, 2021, **405**, 126975.
- 58 Z. Xing, L. Hu, D. S. Ripatti, X. Hu and X. Feng, *Nat. Commun.*, 2021, **12**, 136.
- 59 Z. Cai, Y. Zhang, Y. Zhao, Y. Wu, W. Xu, X. Wen, Y. Zhong, Y. Zhang, W. Liu, H. Wang, Y. Kuang and X. Sun, *Nano Res.*, 2018, **12**, 345–349.
- 60 M. Alfath and C. W. Lee, *Catalysts*, 2020, **10**, 859.
- 61 Y. Yoon, A. S. Hall and Y. Surendranath, *Angew. Chem., Int. Ed.*, 2016, **55**, 15282–15286.
- 62 A. Chen and B.-L. Lin, *Joule*, 2018, **2**, 594–606.
- 63 X. Tan, C. Yu, X. Song, C. Zhao, S. Cui, H. Xu, J. Chang, W. Guo, Z. Wang, Y. Xie and J. Qiu, *Adv. Energy Mater.*, 2021, 2100075.

